AGU PUBLICATIONS

JGR

Journal of Geophysical Research: Space Physics

RESEARCH ARTICLE

10.1002/2014JA020736

One- and two-dimensional hybrid simulations of whistler mode waves in a dipole field

S. Wu[1], R. E. Denton[1], K. Liu[2], and M. K. Hudson[1]

[1]Department of Physics and Astronomy, Dartmouth College, Hanover, New Hampshire, USA, [2]Department of Physics, Auburn University, Auburn, Alabama, USA

Key Points:
- We simulate whistler waves using a hybrid code
- One-dimensional simulations along dipole field agree with nonlinear theory and observation
- Simulations in a meridional plane reveal features of whistler wave propagation

Correspondence to:
S. Wu,
shuo.wu.gr@dartmouth.edu

Citation:
Wu, S., R. E. Denton, K. Liu, and M. K. Hudson (2015), One- and two-dimensional hybrid simulations of whistler mode waves in a dipole field, *J. Geophys. Res. Space Physics*, *120*, 1908–1923, doi:10.1002/2014JA020736.

Received 16 OCT 2014
Accepted 2 FEB 2015
Accepted article online 5 FEB 2015
Published online 20 MAR 2015

Abstract We simulate whistler mode waves using a hybrid code. There are four species in the simulations, hot electrons initialized with a bi-Maxwellian distribution with temperature in the direction perpendicular to background magnetic field greater than that in the parallel direction, warm isotropic electrons, cold inertialess fluid electrons, and protons as an immobile background. The density of the hot population is a small fraction of the total plasma density. Comparison between the dispersion relation of our model and other dispersion relations shows that our model is more accurate for lower frequency whistlers than for higher frequency whistlers. Simulations in 2-D Cartesian coordinates agree very well with those using a full dynamics code. In the 1-D simulations along the dipole magnetic field, the predicted frequency and wave number are observed. Rising tones are observed in the one-fourteenth scale simulations that have larger than realistic magnetic field spatial inhomogeneity. However, in the full-scale 1-D simulation in a dipole field, the waves are more broadband and do not exhibit rising tones. In the 2-D simulations in a meridional plane, the waves are generated with propagation approximately parallel to the background magnetic field. However, the wavefronts become oblique as they propagate to higher latitudes. Simulations with different plasma density profiles across *L* shell are performed to study the effect of the background density on whistler propagation.

1. Introduction

Whistler mode waves are VLF emissions observed in the frequency range between the lower hybrid resonance frequency and electron gyrofrequency, most often with minimum of wave power at 0.5 Ω_{ce}, where Ω_{ce} is the electron gyrofrequency [*Tsurutani and Smith*, 1974; *Burtis and Helliwell*, 1976]. They are excited by the temperature anisotropy of electrons with energy of several to many keVs at the magnetic equator where the electron anisotropy is the largest and then propagate away to high latitudes. The frequency-time spectrum can be either broadband or narrowband, and the narrowband whistler waves are called chorus waves. One distinct feature of chorus waves is that they often display rising or falling tones in the frequency-time structure, which may be related to strong nonlinear growth [*Cully et al.*, 2011; *Helliwell*, 1967].

Whistler mode waves have drawn increasing attention in the space science community. First, they play an important role in both the acceleration and loss of electrons in the radiation belt in the inner magnetosphere [*Thorne*, 2010; *Thorne et al.*, 2013, and references therein]. The lower energy electrons (a few keVs) are responsible for chorus generation, and their temperature anisotropy is relaxed. Some of these electrons will be scattered into the loss cone and precipitated to the ionosphere. On the other hand, electrons can be accelerated by chorus waves through quasilinear diffusion and nonlinear wave-particle resonant interaction. Thus, the whistler wave is a key factor in determining the balance of the electron flux in the radiation belt. Second, a recent study shows that chorus is the driver of pulsating aurora [*Nishimura et al.*, 2010] and diffuse aurora [*Thorne et al.*, 2010]. Third, a recent study using ray tracing shows that chorus waves may be the source of hiss waves in the plasmasphere [*Draganov et al.*, 1992; *Bortnik et al.*, 2008]. Hiss waves play an important role in scattering electrons into the loss cone in the slot region [*Summers et al.*, 2008].

Recent observations discovered large-amplitude whistler waves [*Cattell et al.*, 2008; *Cully et al.*, 2008; *Wilson et al.*, 2011]. These waves have amplitude up to more than 240 mV/m, an order of magnitude larger than previously observed. Most of these waves were observed inside the radiation belt and during magnetically active periods. The wave vectors are up to 50° (mostly within 20°) to the terrestrial magnetic field with a large longitudinal (along the wave vector) electric field component [*Wilson et al.*, 2011]. With the launch

of the Van Allen Probes, fine structure in these waves has been observed. *Santolík et al.* [2014] analyzed a large number of large-amplitude chorus packets with rising tones. They found that the instantaneous wave vectors change by tens of degrees within a single rising tone element with the largest amplitude corresponding to small wave angles. Besides large-amplitude whistler waves, *Santolík et al.* [2009] reported observation in the source region of oblique propagation of whistler mode waves in the regimes of both discrete chorus waves and shapeless hiss waves. *Li et al.* [2011b] presented a comprehensive statistical study of properties of rising and falling tones using Time History of Events and Macroscale Interactions during Substorms (THEMIS) data and found that rising tones tend to be quasi field aligned, whereas falling tones are very oblique close to the resonance cone. Thus, simulations in 2-D dipole field are required to study the generation of falling tones. While most previous work assumes that chorus propagates along the background magnetic field, these discoveries require nonlinear theory and simulations in two dimensions to explain their generation and propagation.

Several self-consistent models of chorus waves have successfully reproduced many features of chorus waves. Using a Vlasov code with a seed wave, *Nunn* [1974] first showed that nonlinear trapping of electrons can trigger the whistler instability. *Trakhtengerts* [1995] and *Trakhtengerts et al.* [2007] applied a generation regime similar to the backward wave oscillator to the generation of whistler chorus emissions. *Katoh and Omura* [2007] developed a one-dimensional electron hybrid code and presented a simulation that self-consistently reproduces the rising tones from thermal noise. *Omura et al.* [2008] further investigated the nonlinear theory and simulation of chorus generation. They emphasized the importance of temporal frequency variation that leads to the formation of rising tones and derived a relation between the frequency sweep rate and wave amplitude. The wave amplitude is amplified due to the spatial inhomogeneity of the dipole magnetic field. *Hikishima et al.* [2009] then performed one-dimensional simulations of chorus with rising tones using a full particle code. Their results support the previous nonlinear theory for chorus generation and frequency sweep rates. *Nunn and Omura* [2012] reproduced a falling tone when their inhomogeneity factor S is positive instead of negative as it is for a rising tone. Recently *Tao* [2014] presented a new electron hybrid code to study the variation of wave intensity with respect to linear growth rate. He demonstrated that a small increase in the linear growth rate will lead to a significant increase in the wave intensity only when the waves are narrow band; thus, nonlinear theory is required to explain the modulation of chorus wave intensity previously observed [*Watt et al.*, 2011; *Wu et al.*, 2013].

Though these simulations have successfully answered many key questions about chorus waves, they have some limitations. First, the one-dimensional background magnetic field is approximated by an azimuthally symmetric parabolic field. Second, due to the high computational cost, these simulations often assumed a scaled-down system with the magnetic field spatial inhomogeneity larger than the real system. A comparison between different scaled-down systems is important for understanding the effect of magnetic field inhomogeneity on chorus waves [*Katoh and Omura*, 2013; *Tao et al.*, 2014]. In addition, all of these preceding simulations are one-dimensional along an inhomogeneous magnetic field; they thus assume that the waves propagate only along the field. Two-dimensional simulations with a straight magnetic field have also been performed to study wave excitation [*Liu et al.*, 2011a, 2011b; *Woodroffe and Streltsov*, 2014, and references therein]. While these simulations have important implications for magnetospheric whistlers, they lack the spatial inhomogeneity in the background magnetic field which is essential for the generation of rising tones. And to address the generation and propagation of oblique whistler waves, two-dimensional simulations in a meridional plane are needed.

The propagation of whistler waves is a challenging topic. Ray tracing is an efficient technique to study whistler propagation. The refractive index of whistler waves depends on both cold plasma density and the background magnetic field as they control the wave dispersion relation [*Gendrin*, 1961; *Helliwell*, 1965; *Inan and Bell*, 1977]. *Chen et al.* [2009] studied the whistler wave path in a three-dimensional magnetosphere with azimuthal density variation including a plasmaspheric plume. They found that pronounced off-meridian propagation is more effective inside the plasmasphere than outside due to internal reflection from the plasmapause. These results suggest that outside the plasmapause, a two-dimensional simulation of whistler waves in the meridional plane could be appropriate to investigate wave growth and propagation. *Katoh* [2014] recently showed simulations of the propagation of chorus in a meridional plane. They showed how chorus elements propagate on different raypaths depending on the density variation. In their simulations, waves with rising tones are artificially inserted into the simulation domain.

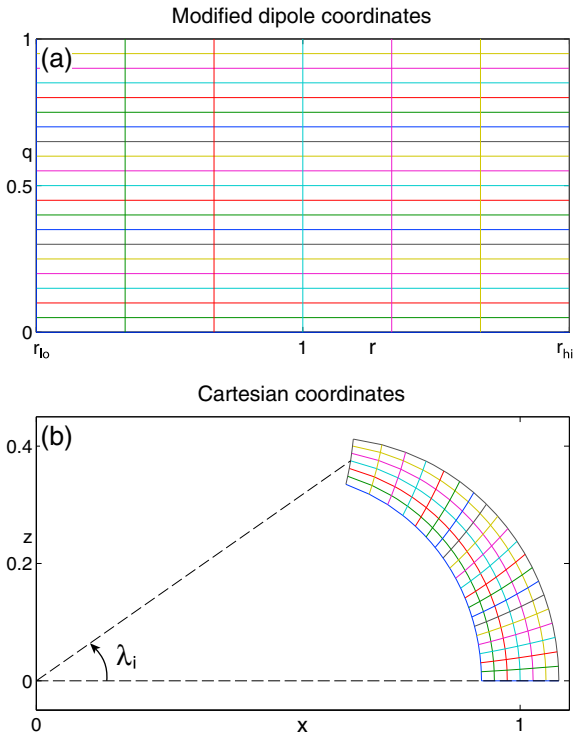

Figure 1. (a) Modified dipole coordinates (q, r) and (b) the mapping to the Cartesian coordinates (z, x); x and z are the SM X and Z coordinates in the noon meridional plane. The magnetic latitude of the northern boundary is λ_i.

In this manuscript, we present simulations of whistler mode waves using a hybrid code in dipole coordinates. First, we compare the dispersion relation in our model with results form a local dispersion relation solver. Then we present simulations in 2-D Cartesian, 1-D dipole, and 2-D dipole systems. In our simulations, waves are excited by anisotropic electrons and grow from thermal noise. We also perform simulations in a way similar to *Katoh* [2014], where we input a traveling whistler wave into a meridional plane and investigate wave propagation. Our simulations reproduce many features of whistler mode waves generation and propagation and are to our knowledge the first self-consistent first-principle simulations including wave growth in a two-dimensional meridional plane.

2. Model for Whistler Mode Waves

Our hybrid code has successfully simulated two-dimensional electromagnetic ion cyclotron (EMIC) waves [*Hu et al.*, 2010]. In such simulations, ions are treated as particles and the electrons as a cold fluid without mass. We slightly modified the equations in the hybrid code to allow simulation of whistler waves. Whistler waves can be excited by temperature anisotropy of ring current electrons, just like EMIC waves are stimulated by the temperature anisotropy of the ions [*Kennel and Petschek*, 1966].

2.1. Hybrid Code

Our hybrid code uses generalized orthogonal coordinates. Thus, we can test the simplest case of whistler waves in Cartesian coordinates as well as simulate magnetospheric waves in dipole coordinates. We will use the modified dipole coordinates (q, r, s) introduced by *Hu and Denton* [2009]. Simply put, the first coordinate, q, is a measure of the distance along field lines; r is the L shell, normalized to the L value at the center ($r = 1$); and s is the azimuthal angle. Figure 1 shows the modified dipole coordinates and the mapping to Cartesian coordinates in the meridional plane where $s = 0$; $q = 0$ represents the equatorial plane and $q = 1$ represents the Northern Hemisphere ionospheric boundary. Note that our ionospheric boundary is not at the real ionosphere but is at a higher latitude; it is specified by its magnetic latitude λ_i at $r = 1$. The modified dipole coordinates have several advantages. We choose to make the spacing between grid points in the q direction roughly proportional to the magnetic field B, which is proportional to the electron Alfvén speed V_{Ae}. Then the spacing between grid points in real space is the largest close to the ionospheric boundary, where B is large. This helps to ameliorate problems with the Courant condition (numerical stability condition related to temporal resolution of waves) near the ionospheric boundary. Second, the number of particles per cell will be roughly constant along the field line. This is because the area of a flux tube is proportional to $1/B$ and the length of the cell is proportional to B so that the grid cell volume is roughly constant along a field line.

Our code can utilize various boundary conditions depending on the physical problem of interest. In the simulation in 2-D Cartesian coordinates that aims to compare the results with linear theory, we used periodic boundary conditions in both directions. In both 1-D and 2-D dipole coordinates, we performed simulations only in the Northern Hemisphere ($q > 0$) to reduce the computational cost, and symmetry boundary conditions are used at the magnetic equator. At other boundaries, perfect conductor boundary conditions were used for the fields as discussed by *Denton and Hu* [2009], and particles were reflected as described by

Table 1. Basic Equations Used in the Hybrid Code[a]

$\frac{d\mathbf{x}_m}{dt} = \mathbf{v}_m$
$\frac{d\mathbf{v}_m}{dt} = -\mathbf{E}_m - \mathbf{v}_m \times \mathbf{B}_m - \eta \mathbf{J}_m$
$\rho_{t,i} = \frac{1}{H_i} \Sigma_m Q_m S\left(\mathbf{x}_i - \mathbf{x}_m\right)$
$n_{e,c,i} = n_{\text{ion},i} - n_{e,t,i}$
$\mathbf{J}_{t,i} = \frac{1}{H_i} \Sigma_m Q_m \mathbf{v}_m S(\mathbf{x}_i - \mathbf{x}_m)$
$\frac{\partial \mathbf{B}_i}{\partial t} = -\nabla \times \mathbf{E}_i$
$\mathbf{J}_i = \nabla \times \mathbf{B}_i$
$\mathbf{u}_{e,c,i} = -\frac{1}{n_{e,c}}(\mathbf{J}_i - \mathbf{J}_{e,t,i})$
$\mathbf{E}_i = -\mathbf{u}_{e,c,i} \times \mathbf{B}_i + \eta \mathbf{J}_i$

[a]The subscripts *m* and *i* are the particle index and grid index, respectively; *t* denotes thermal particles with mass; *c* denotes the inertialess cold fluid species; and *e* is for electron.

Lee and Okuda [1978] and *Naitou et al.* [1979]. We also added a resistive layer and masking function at the boundaries (except the magnetic equator) to reduce the undesired waves (see section 2.3 in *Hu and Denton* [2009]). These conditions ensure total energy conservation if we take into account the energy lost at the resistive boundaries.

We initialized the plasma with an anisotropic MHD code [*Hu et al.*, 2010], such that the initial state of the simulation is nearly MHD equilibrium. Undesired wave modes due to nonequilibrium oscillations are thus removed from our system, and the noise is reduced. The adjusted magnetic field lines are nearly though not exactly dipolar.

The full set of basic equations is listed in Table 1. Each quantity is normalized as described in Table 2. The fluid velocity of the cold electrons is $\mathbf{u}_{e,c} = -\left(\mathbf{J} - \sum_s \mathbf{J}_s\right)/(n_{e,c}e)$, where $\mathbf{J}_s$ is the current of particle species and $\mathbf{J} = \nabla \times \mathbf{B}$ is the total current. The immobile ions have zero current. We then make the approximation that the cold electrons are able to short out the parallel electric field and undergo $\mathbf{E} \times \mathbf{B}$ drift, providing an explicit equation for $\mathbf{E}$, i.e., $\mathbf{E} = -\mathbf{u}_{e,c} \times \mathbf{B}$. In Table 1, the subscript *e* indicates electrons, *m* and *i* represent the particle index and grid index, respectively, Q_m is the charge of the *m*th super particle, $H_i = h_{1i}h_{2i}h_{3i}$ is the product of the scale factors of the *i*th grid cell, and $S(\mathbf{x}_i - \mathbf{x}_m)$ is the shape function of super particles.

2.2. Model for Whistler Mode Waves

In our simulations of whistler waves, we include four species. Energetic anisotropic electrons (ring current electrons) are treated as particles to stimulate the instability. These electrons only make up a small fraction of the total electron population. Warm particle electrons are included to make the dispersion relation more accurate by increasing the fraction of particles with mass. These electrons are initially isotropic. Cold inertialess electrons are treated as a fluid. Finally, the ions are represented as fixed background positive charge density. With these assumptions, our model has some advantages as well as limitations. Because we use the drift motion of cold inertialess electrons to obtain the electric field, we exclude the displacement current, eliminating light waves from the simulation. We also assume that there is a large population of cold electrons so that f_{pe} exceeds f_{ce}, where f_{pe} is the plasma frequency and f_{ce} is the electron gyrofrequency. Then in the real system, the parallel electric field $E_\parallel$ would be small. In our simulation, the inertialess electrons move freely along the magnetic field to exactly cancel $E_\parallel$. In this way, Langmuir wave is eliminated from the system, but its effect on $E_\parallel$ is included. The approximation $E_\parallel = 0$ is valid in the limit of large f_{pe}/f_{ce} for $\theta_{kB} < 90^o$, where θ_{kB} is the angle between the wave vector and background magnetic field. Because the electron inertia makes the dispersion surface asymptote to $\omega = \Omega_{ce}$ and the inertia is less important for low frequencies, our results will also be more accurate for lower band chorus than for upper band chorus (see Figure 2 in later discussions). But lower band chorus is dominant in the space observations,

Table 2. Normalizations in the Hybrid Code

Quantity	Normalized to
Mass	$m_0 = m_e$
Charge	$q_0 = e$
Magnetic field	B_0
Velocity	$V_{Ae0} = B_0/\sqrt{4\pi m_e n_{e0}}$
Time	$t_0 = \Omega_{e0}^{-1}$
Length	$x_0 = c/\omega_{pe0}$
Number density	$n_0 = n_{e0}$
Charge density	$\rho_0 = n_{e0}e$
Current density	$J_0 = n_{e0}eV_{Ae0}$
Electric field	$E_0 = V_{Ae0}B_0/c$
Resistivity	$\eta_0 = 4\pi V_{Ae0}^2/(c^2\Omega_{e0})$
Temperature	$T_0^2 = B_0^2/(4\pi n_{e0})$
Pressure	$p_0 = B_0^2/(4\pi)$

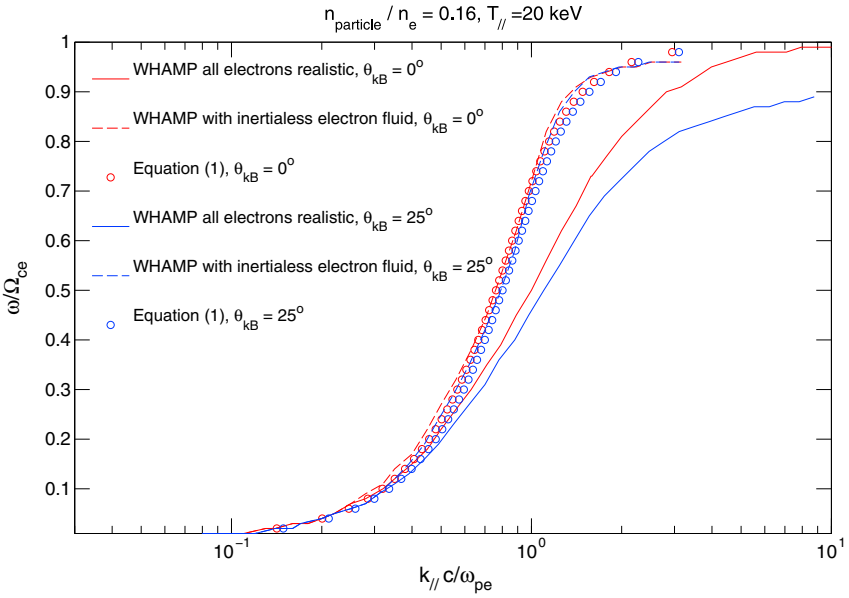

Figure 2. Comparison of the dispersion relation of our model (1) and WHAMP for $\theta_{kB} = 0°$ (red color) and $\theta_{kB} = 25°$ (blue color). The figure shows normalized frequency versus normalized wave vector. Solid lines represent WHAMP with realistic mass electrons, while dashed lines represent results with inertialess electrons. Circles denote the model used in the hybrid code. For this comparison, the particle electrons that always have realistic mass are 16% of the total electron population and the parallel temperature is 20 keV.

for example, the statistical study from THEMIS [*Cully et al.*, 2008]. For these reasons we will focus on lower band chorus.

Equation (1) is the cold plasma dispersion relation derived using the equations listed in Table 1.

$$\bar{n}_c^2\bar{\omega}^4 - \bar{\omega}^2(1 + (1 - \bar{n}_c)\bar{k}^2(1 + \cos^2\theta_{kB}) + \bar{k}^4\cos^2\theta_{kB}) + \bar{k}^4\cos^2\theta_{kB} = 0, \tag{1}$$

where $\bar{n}_c$ is the density of cold inertialess electrons normalized to the total electron density n_e, $\bar{\omega} \equiv \omega/\Omega_{ce}$, and $\bar{k} \equiv kc/\omega_{pe}$. In various limits, (1) reduces to familiar relations. For example, if there is only a cold population in our simulation ($\bar{n}_c = 1$), (1) becomes

$$\bar{k}\bar{k}_{\|} = \bar{\omega}, \tag{2}$$

which is the cold dispersion relation for whistler waves in the low-frequency limit, where $\bar{k}_{\|} = \bar{k}\cos\theta_{kB}$ is the parallel component of $\bar{k}$. If there is no inertialess population ($\bar{n}_c = 0$), a case which our hybrid code cannot run because of numerical instability, (1) reduces for parallel propagation ($\theta_{kB} = 0$) to

$$\bar{k}_{\|}^2 = \frac{\bar{\omega}}{1 - \bar{\omega}}, \tag{3}$$

the cold dispersion relation for whistler waves including the resonance at the electron gyrofrequency. For purely parallel propagation with electrons both with and without mass, (1) becomes

$$\bar{k}_{\|}^2 = (1 - \bar{n}_c)\frac{\bar{\omega}}{1 - \bar{\omega}} + \bar{n}_c\bar{\omega}. \tag{4}$$

The first term on the right-hand side of (4) is the contribution from the particle electrons with mass in the high-frequency regime (when $\bar{\omega}$ is very small, this term becomes similar to the second term), while the second term is from the inertialess distribution. Note that if we solve (1) for ω^2 as a function of k, we get two solutions. For one solution $\bar{\omega}$ is between 0 and 1 representing the whistler wave. For the other solution, $\bar{\omega}$ goes from 1 to infinity, representing an artificial wave due to the inertialess electrons (see later discussion). These two branches are analogous to ion cyclotron wave with multiple species, where different dispersion curves approach the gyrofrequency of different species. In our model, the whistler branch approaches the electron gyrofrequency, while the artificial branch approaches the gyrofrequency of the inertialess electrons, which is infinite.

We compared (1) with dispersion surfaces calculated using the electromagnetic dispersion code WHAMP (Waves in Homogeneous, Anisotropic Multicomponent Plasmas), originally developed by Kjell Ronnmark [*Ronnmark*, 1983]. Figure 2 shows the dispersion curves for the parameters used in our simulations. The values of $\bar{k}$ range from 0.1 to 10, which is the relevant regime for whistler waves. All the red curves denote results for parallel propagating whistler waves, while the blue curves are for $\theta_{kB} = 25^o$. The solid curves are for WHAMP for all electrons with realistic mass, while the dashed curves are for WHAMP with electron mass for the fluid component equal to $10^{-10}\, m_e$ (m_e is the mass of electrons), which is effectively zero, and the circles represent results from (1). The fraction of the particle electrons that always have mass is 16%, which is a typical value for our simulation. The parallel temperature of the particle population is 20 keV. Note that all the curves asymptote to a resonance at the electron gyrofrequency. With more realistic mass electrons (as denoted by the two solid curves), the frequency is lower at any $\bar{k}$ and the frequency approaches the gyrofrequency at larger $\bar{k}$. The difference in $\bar{k}$ between (1) and WHAMP with all realistic mass electrons for $\theta_{kB} = 25^o$ is about 17.5% at $\bar{\omega} = 0.4$. Third, the four curves with inertialess electrons are very close to each other, indicating that our model agrees very well with WHAMP with inertialess electrons. In addition, there is not much difference between the dispersion curves for parallel and oblique propagation when most electrons are inertialess, while the difference is clear when all electrons have realistic mass comparing the two solid curves. Figure 2 demonstrates that our model is more accurate for low frequency for which the inertia becomes less important.

Besides using a population of inertialess electrons, our model also assumes that $E_\parallel$ is equal to zero. If f_{pe} is smaller than f_{ce}, $E_\parallel$ will not be shorted out on the timescale of whistler waves. However, most observations find that the typical ratio of f_{pe} to f_{ce} is 4 to 7. Also, for θ_{kB} almost equal to 90°, the electrons will not be able to move freely along the magnetic field, and thus $E_\parallel$ cannot be canceled in this case either. Our model will fail to be valid if the parallel component of the wave electric field $E_\parallel$ becomes a large fraction of E. The fact that *Cattell et al.* [2008] found $E_\parallel \sim 0.1E$ suggests that our model may be sufficient for an approximate description of their results.

3. Simulation Results

3.1. Parameters

The Geospace Environment Modeling Radiation Belts and Wave Modeling focus group chose a set of parameters for a comparison study, or challenge. We used the same parameters as this challenge except that we used 10 times larger hot electron density. For the hot electrons, $n_{hot} = 0.33\ cm^{-3}$, $T_{hot} = 20$ keV, $T_\perp/T_\parallel = 3$. The warm population have $n_{warm} = 0.55\ cm^{-3}$, $T_{warm} = 0.01$ keV, and $T_\perp/T_\parallel = 1$. For the cold inertialess fluid electrons, $n_{cold} = 4.62\ cm^{-3}$. The total plasma density n_e is hence $5.5\ cm^{-3}$. The background magnetic field B_0 is 250 nT. Hence, the parallel plasma beta of the hot population is $\beta_{\parallel,hot} = 0.04$. With these parameters, the most unstable mode propagates in the parallel direction. Equation (1) predicts that for the most unstable mode, $\bar{\omega} = 0.4$, $\bar{\gamma} = 0.03$, $\bar{k}_\parallel = 0.68$, and the normalized wavelength $\bar{\lambda}_\parallel = 9.24$. For such parameters WHAMP predicts that $\bar{\omega} = 0.36$, $\bar{\gamma} = 0.02$, $\bar{k}_\parallel = 0.76$, and $\bar{\lambda}_\parallel = 8.27$. The normalizing factors are $\Omega_{ce} = 4.4 \times 10^4$ rad/s ($f_{ce} = 7$ kHz), $\omega_{pe} = 1.3 \times 10^5$ rad/s ($f_{pe} = 21$ kHz), and $c/\omega_{pe} = 2.27$ km.

We performed simulations with different geometry and density variation. First, we simulated the waves in 2-D Cartesian coordinates (run 1) and compared the results with those of a full dynamics particle-in-cell simulation to examine the validity of our model. Then we ran two simulations in 1-D dipole geometry, one in full-scale system (run 2) and one in a scaled-down system (run 3). Finally, we ran simulations in 2-D dipole geometry with different plasma density profiles across L shell (runs 4–6) and compared the results with cold plasma simulations (runs 7–9). The parameters of each simulation are listed in Table 3.

3.2. Two-Dimensional Test Simulation in Cartesian Coordinates

To test the validity of our model, we first performed a two-dimensional simulation in Cartesian coordinates. The background magnetic field is constant in the z direction. The simulation size is $10\bar{\lambda}_\parallel$ times $10\bar{\lambda}_\perp$, where $\bar{\lambda}_\parallel$ and $\bar{\lambda}_\perp$ are the normalized wavelengths in the parallel and perpendicular directions based on predictions from WHAMP. The strongest instability for **k** is in the parallel direction for which $\bar{\lambda}_\perp$ would be infinity. We chose $\bar{k}_\perp$ such that the growth rate is half of the maximum growth rate, and the corresponding $\bar{k}_\perp$ is 0.37; thus, $\bar{\lambda}_\perp$ is 16.98. Hence, the normalized length in z is 92 and that of x is 170. We compared the results with a full dynamics simulation using the 2-D electromagnetic particle-in-cell code in *Liu et al.* [2011a, 2011b]. The full dynamics code includes physics that is absent in our model, for example, the displacement current and

Table 3. Summary of the Settings and Key Parameters of the Simulations[a]

Run	N_q	N_r	N_P	λ_i	$L_0\omega_{pe}/c$	Density Variation
1	256	256	3000	na	na	na
2	10001	1	400	23°	14031	na
3	953	1	400	23°	1000	na
4,7	953	151	560	23°	1000	constant
5,8	953	151	560	23°	1000	L^{-4}
6,9	953	151	560	23°	1000	L^{-8}

[a] N_q and N_r are the number of grid points in q and r, respectively. N_P is the number of particles per cell. The magnetic latitude of northern ionospheric boundary is λ_i. $L_0\omega_{pe}/c$ is the normalized value of L shell at the middle of the simulation.

realistic mass for all electrons. To do the comparison, we performed the simulations with the same parameters for the hot population and warm population. To approximate the cold inertialess electrons in our hybrid code, Liu's model used a particle electron population with temperature equal to 0.01 eV. In both simulations, the grid size was 256 × 256. In the hybrid code, there were 3000 particles per grid cell in total for the two particle populations, while in the full particle code, there were 1000 particles per grid cell representing each of the three electron populations. Periodic boundary conditions were used in both directions.

Figure 3 plots the perturbed magnetic energy versus time in both models. The perturbed magnetic energy is defined as $< |\delta\mathbf{B}|^2 > /B_0^2$, where B_0 is the amplitude of background magnetic field and $\delta\mathbf{B}$ is the perturbed magnetic field, and <> indicates an average over the grid. The red curve denotes results from the hybrid code, while the black curve is for the full particle code. In both models, the energy undergoes equilibration of modes to the noise level followed by a linear growth stage and then followed by a nonlinear growth stage. Note that, with the same number of particles per cell with the hybrid code, the full dynamics particle code yields a lower noise level due to the fact that it uses the quiet start technique to initialize particles with a reduced thermal fluctuation level. For the full dynamics code, the growth rate is around 0.02 as predicted by WHAMP, while in the hybrid code, it is 0.03. The normalized magnetic field energy saturation level is comparable, 0.0027 for the hybrid code, 0.0024 for the full dynamics code. The hybrid code yields a slightly higher saturation level due to larger growth rate.

Figure 4 compares the out-of-plane component B_y of the wave magnetic field and the power spectrum in k space just after the waves are saturated. Note that in Figures 4a and 4b, the x axis is compressed relative to the z axis. Looking at Figures 4a and 4b, we see that in the z direction, there are about nine peaks (darkest red) and nine troughs (darkest blue). Thus, the wavelength is about one ninth of the distance across z, which is very close to the prediction of linear theory. In fact, at an earlier stage of the simulation, when the electron parameters have not evolved much from the initial values, there are 10 wavelengths in the parallel direction. Thus, the dominant wave energy has shifted slightly to smaller k (inverse cascade) associated with the evolution of the electron parameters in the simulation. The anisotropy of the hot electron population decreases as the instability develops, which, according to linear dispersion theory, shifts the most unstable wave mode toward smaller k or longer wavelength. So there will be fewer and fewer wavelengths in the parallel direction later in the simulation. In the perpendicular direction, there are about four wavelengths in both simulations. After performing a Fourier transform on the magnetic field in Figures 4a and 4b,

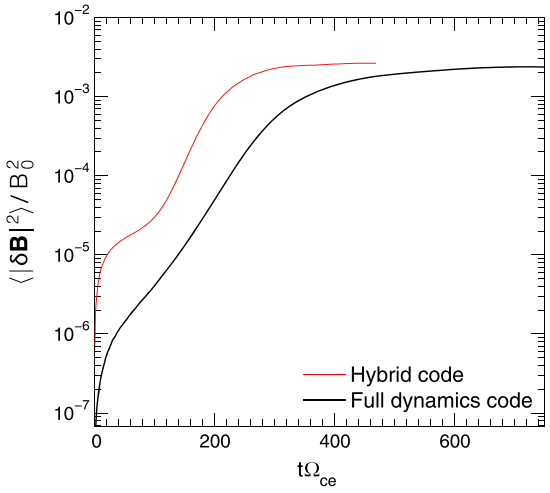

Figure 3. Perturbed magnetic energy versus time for the hybrid code (red curve) and full dynamics code (black curve).

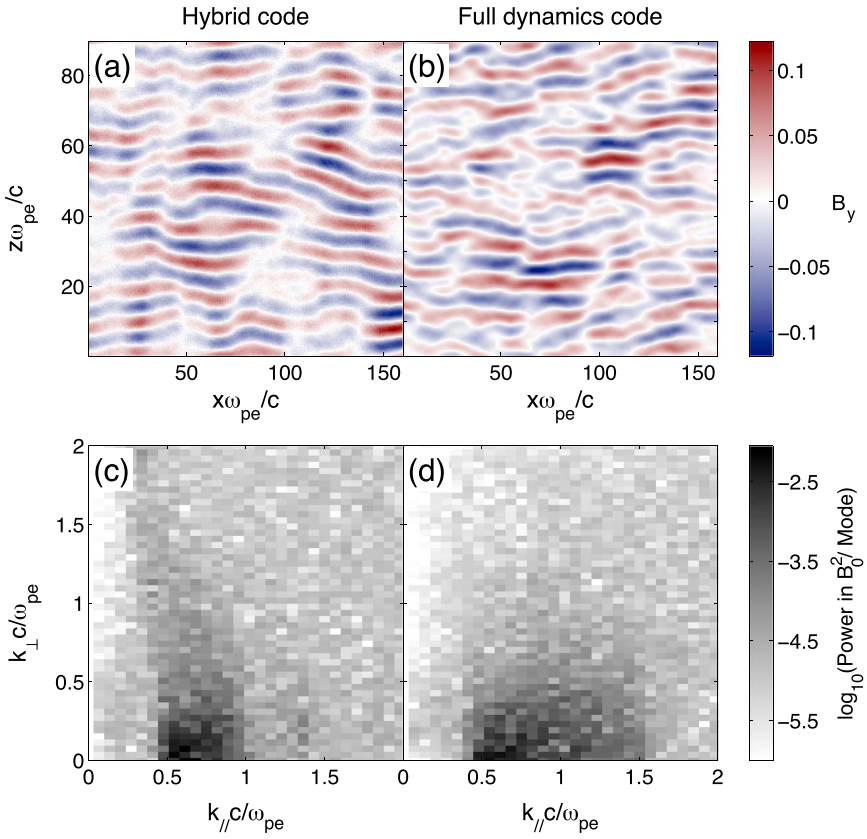

Figure 4. At the top, a snapshot of the out-of-plane component B_y of wave magnetic field just after saturation for (a) the hybrid code and (b) the full dynamics code. At the bottom, the wave number power spectra of the out-of-plane magnetic field component in logarithmic scale (gray scale) for (c) the hybrid code and (d) the full dynamics code.

we find the power spectrum that we display in Figures 4c and 4d. For both simulations, most of the wave power is in the parallel direction corresponding to $\bar{k}_\perp = 0$. The wave power is mostly between $\bar{k}_\parallel = 0.5$ and 1, which agrees with the prediction by WHAMP. Again, the largest power is not at $\bar{k}_\parallel = 0.7$ as predicted by WHAMP but smaller due to the fact that k decreases as the anisotropy decreases. The maximum power in Figure 4c is slightly greater (the color is slightly darker). The greatest difference is in the k range of instability. Figure 4d shows that the full dynamics simulation has a larger unstable region in $k_\parallel$. But our model agrees qualitatively very well with the full dynamics code.

We then analyzed the power spectrum in ω-k space. To do this, we Fourier transformed the complex field $S = B_x + iB_y$. Then positive frequency corresponds to right-hand polarized modes, while negative frequency corresponds to left-hand polarized modes. The waves propagate in the positive direction of a coordinate j if the sign of k_j matches that of ω. Figure 5 shows the power spectrum for the Cartesian simulations using the hybrid code when $t\Omega$ is between 300 and 400. There are three branches. The middle branch, in which $\bar{\omega}$ goes from 0 to 1, is the whistler dispersion surface; most of the wave power in this branch is between $\bar{\omega} = 0.25$ and 0.75. The positive frequency indicates that these waves are right-hand polarized. The surface approaches $\bar{\omega} = 1$ due to the resonance of the particle electrons. The upper branch, where $\bar{\omega}$ goes from 1 to higher values, represents the artificial surface due to inertialess electrons as discussed in the previous section. Finally in the lowest branch, the frequency is negative. These waves are left-hand polarized and combine with the corresponding right-hand polarized waves to form waves that are nearly but not completely right-hand polarized. In all three branches, the wave power is almost evenly distributed between positive and negative $k_\parallel$ because the waves are traveling in both directions (the simulation system is symmetric). The power of the upper and lower branch is much smaller than that of the middle branch (The color bar spans about 5 orders of magnitude). Note that there is some very small power in the two lower corners, which is due to the aliasing of the high frequencies.

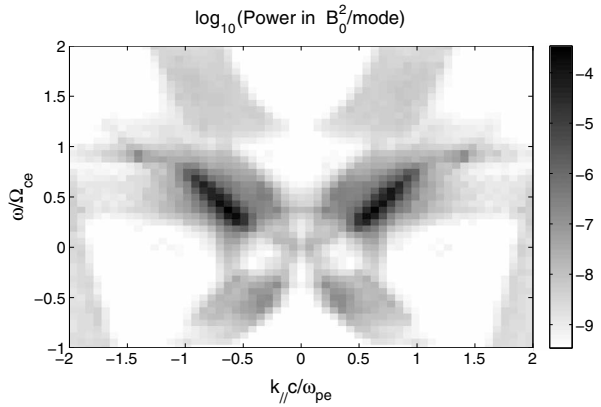

Figure 5. Wave power versus $\bar{k}_{\|}$ on the horizontal axis and $\bar{\omega}$ on the vertical axis for the time range $t\Omega_{ce} = 300$ to 400. Positive (negative) frequency denotes waves with right (left)-hand polarization. If the sign of $\bar{k}_{\|}$ matches that of $\bar{\omega}$, the waves propagate in the positive direction of the parallel direction z.

Overall, our results agree very well with Liu et al.'s model, and the comparison shows that our model is capable of representing the physics needed for whistler wave generation.

3.3. One-Dimensional Simulations in Dipole Geometry

We simulated waves with the parameters listed in the previous section in dipole geometry in both full-scale and scaled-down systems. For both simulations, q goes from 0 to 1, with 1 corresponding to the northern boundary at magnetic latitude (MLAT) = 23°. In reality, the wavelength of the most unstable mode is 18.77 km for our parameters. Hence, there are about 340 wavelengths in 1 R_e, where $R_e = 6370$ km is the Earth radius. At $L = 5$, MLAT at 1 R_e is about arctan(1/5) = 11.3°. Going up to 23° is sufficient for whistler simulation as the wave power is mostly confined within low magnetic latitudes [*Li et al.*, 2011a]. For the full-scale simulation, we simulated a distance of about 2 R_e, so there are about 680 wavelengths. We used 10,001 grid points in the q direction to resolve these modes. Then on average, there are about 15 grid points for each wavelength, which is enough to resolve the waves. The magnetic field strength increases by a factor of 2 at $q = 1$ from the equatorial value at $q = 0$. The middle L value is $L_0\omega_{pe}/c = 14031$. The scaled-down simulation is one-fourteenth scale, so value of $L_0\omega_{pe}/c$ is 1000. Subsequently, the gradients of the equilibrium quantities in the scaled-down system are 14 times larger than realistic.

Figure 6 shows the results along the 1-D dipole field. Figures 6a and 6b show the azimuthal component of the magnetic field B_ϕ versus q at $t\Omega_{ce} = 150$ in the full-scale and scaled-down systems, respectively, runs 2 and 3. Figures 6c and 6d show the power spectrum along q for the same runs in the time range between $t\Omega_{ce} = 100$ and 200. Looking at Figure 6a, the wave amplitude is the greatest in the region between $q = 0$ and $q = 0.2$ near where the waves are generated and gradually decreases with q. At later times this wave packet propagates to higher q and the wave amplitude continues to grow. If we plot B_ϕ at a later time, then the greatest amplitude is at an off-equator position rather than near the equator (similar to Figure 6b). Between $q = 0.9$ and 1, the magnitude of B_ϕ is nearly zero because of the resistive layer near the boundary. The amplitudes of the waves in the two simulations are quite close. These plots show that the wave power is mostly between $\bar{\omega} = 0.3$ and 0.6. The detailed structure of the power spectrum, however, is hard to see due to the huge number of grid points. This structure is more obvious in run 3. In Figure 6b, there are several wave packets. These are generated continuously at the magnetic equator. Zooming in to the region near the equatorial plane, we find that the normalized wavelength (not shown here) is about 0.025. Based on the linear theory, there should be about 48 wavelengths in the one-fourteenth scaled system in the distance of about 2 R_e and the wavelength should be 0.021, so the wavelength obtained from Figure 6b agrees well with our linear estimation. In Figure 6d, the power is the strongest between $q = 0.2$ and 0.4, corresponding to the peak in amplitude between $q = 0.2$ and 0.3 in Figure 6b. The power in this wave packet is greatest near $\bar{\omega} = 0.4$. There is a second prominent wave packet near $q = 0$ corresponding to the peak in amplitude near $q = 0$ in Figure 6b.

Figure 6d displays a negative frequency gradient along q in the power spectrum. The waves are propagating to the right away from the magnetic equator where they are generated. At a fixed position in space, for example, at $q = 0.4$, the waves with lower frequency will be observed first, then the waves with higher frequency. Thus, a rising tone is expected [*Katoh and Omura*, 2007], and, though not shown here, we observed a rising tone in the frequency-temporal structure near the magnetic equator (not shown). The frequency of the rising tone goes from 0.32 Ω_{ce} to 0.57 Ω_{ce} in a time period of $t\Omega_{ce} = 40$. The frequency sweep rate is thus $6.25 \times 10^{-3}\ \Omega_{ce}^2$, which is greater than that of realistic chorus waves by about 2 orders of magnitude. The huge difference may be due to the large amplitude. *Omura et al.* [2008] gives an equation

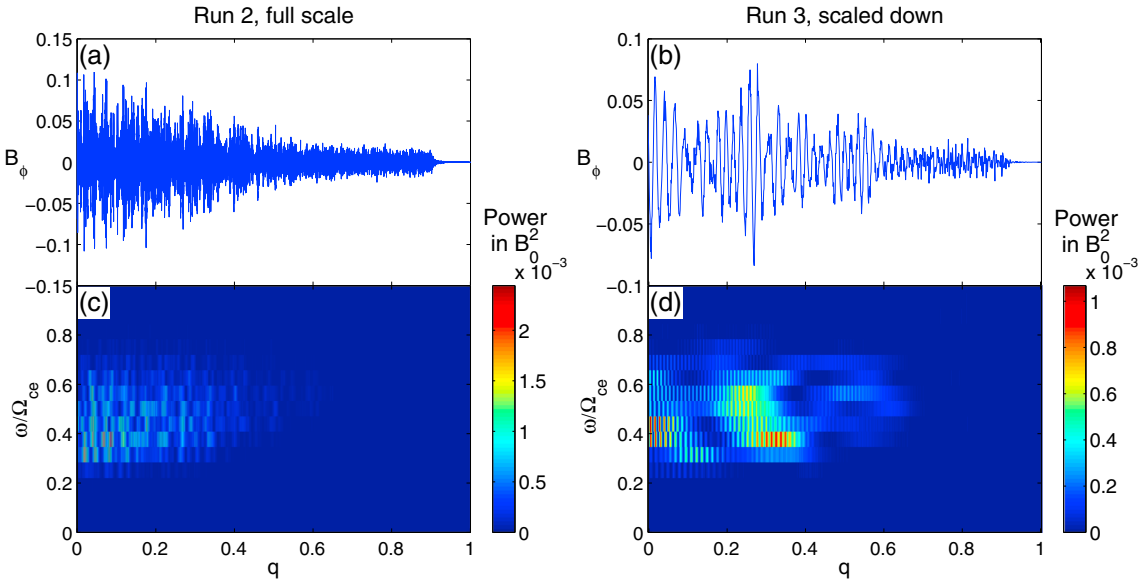

Figure 6. Simulations in 1-D dipole geometry in the (a and c) full-scale system and (b and d) scaled-down system. Figures 6a and 6b show the azimuthal component of the magnetic field at $t\Omega_{ce} = 150$ versus q, and Figures 6c and 6d show the wave power versus q on the horizontal axis and $\bar{\omega}$ on the vertical axis for the time range $t\Omega_{ce} = 100$ and 200.

for the estimation of frequency sweep rate and shows that the sweep rate is proportional to the normalized wave amplitude. We estimated the frequency sweep rate in our simulation based on equation (50) in *Omura et al.* [2008]. For our parameters, we obtained a relation between frequency sweep rate and wave amplitude:

$$\frac{\partial \omega}{\partial t} = 0.1064 \frac{B_w}{B_0} \Omega_{ce}^2, \tag{5}$$

where B_w is the wave amplitude. Based on Figure 6b, B_w is around 0.05; thus, the frequency sweep rate should be $5.32 \times 10^{-3}\ \Omega_{ce}^2$, so the sweep rate we obtained from the simulation agrees with this estimation ($6.25 \times 10^{-3}\ \Omega_{ce}^2$) very well. However, in the full-scale simulation, we did not find a rising or falling tone. The structure of the power spectrum along q in run 2 is much more broadband, and it is hard to find a similar negative gradient of frequency with respect to position in this case.

3.4. Two-Dimensional Simulations in a Meridional Plane

We then extended the simulation to a meridional plane. All the 2-D simulations have the same simulation size. The magnetic latitude of the northern ionosphere boundary at $q = 1$ for the middle L shell is 23°. For the middle L shell $L_0\omega_{pe}/c = 1000$. The r boundaries are 0.92 and 1.08, corresponding to a range of $0.16 \times 1000\, c/\omega_{pe} = 363.2$ km. Note that we are simulating a very narrow range in L shell. There are 953 grid points in q and 151 grid points in r. The r grid spacing is $1.05\, c/\omega_{pe}$, while the cyclotron radius is $1.43\, c/\omega_{pe}$. This resolution is sufficient to resolve the wavelength and gyromotion of particle electrons. The total number of simulation particles used to represent the hot and warm electron populations is 560 per grid cell.

The plasma density controls the dispersion relation of whistler waves and hence the wave propagation. To study the wave propagation with respect to L shell in different plasma density profiles, we set the plasma density constant or varying as L^{-4} or L^{-8}. The plasma density at the central L shell ($r = 1$) is set to be 5.5 cm^{-3}, as mentioned previously.

Figure 7 shows the out-of-plane component of wave magnetic field versus q and r at $t\Omega_{ce} = 100$ (a–c), $t\Omega_{ce} = 200$ (d–f), and $t\Omega_{ce} = 300$ (g–i). The different columns show the results for different plasma density profiles, as indicated at the top of each column. Note that we trimmed the r boundaries to show only the region without the resistive layers (the region plotted is from $r = 0.936$ to 1.064). Within the resistive layers, the amplitude is almost zero and the plot yields little information. Looking at Figures 7a, 7d, and 7g (run 4), we can see that the waves are generated near the equatorial plane and propagate toward larger q (higher latitude). The amplitude grows slightly as the waves propagate as can be seen by comparing the color bars on the right. The direction of k also changes. Note that k is perpendicular to the wavefronts. In Figures 7a–7c,

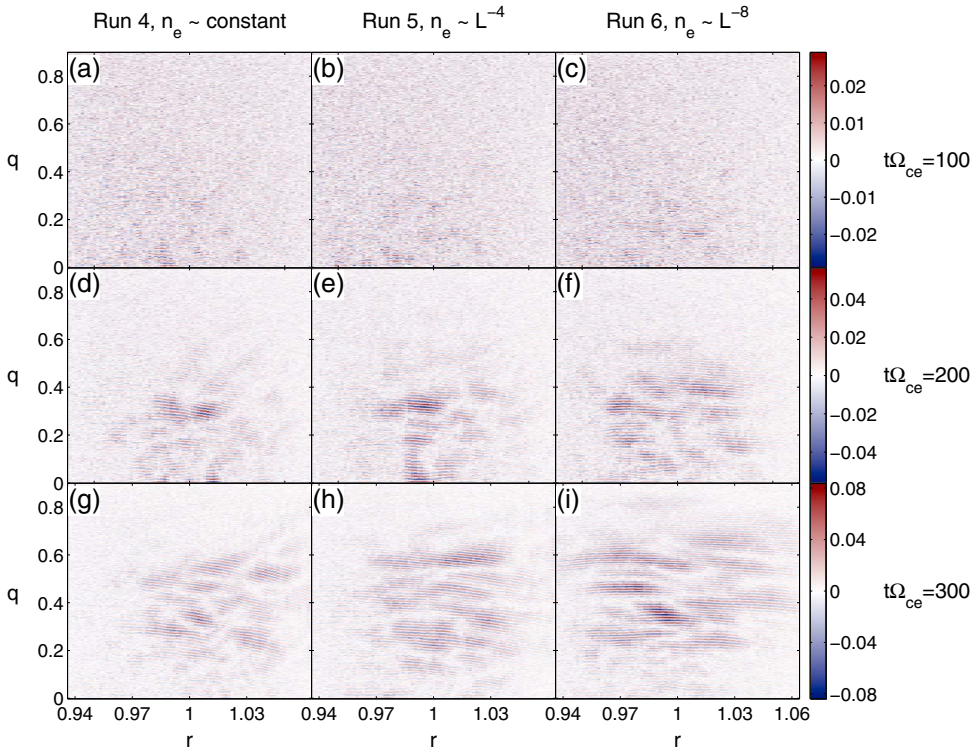

Figure 7. Two-dimensional simulations in dipole geometry with waves self-consistently driven by a hot anisotropic electron population. The figure shows the out-of-plane (azimuthal) component of **B**. (a, d, and g) The results for plasma density n_e = constant at the times indicated at the right of each row, (b, e, and h) results for n_e varying as L^{-4}, and (c, f, and i) results for n_e varying as L^{-8}. Only the r range without wave damping is shown here.

k is pointing parallel to q. In Figures 7d–7f, away from the magnetic equator, k starts to turn away from the q direction (vertical in the figure). Note that at $q = 0$ the background magnetic field is exactly along the q direction; at $q > 0$, the background magnetic field direction is close to though not exactly the same as the q direction. Finally, in the last row, k becomes very oblique near the boundaries. The greatest angle between the wavefront and B is about 45°.

By comparing the plots in different columns, we can see the effects of the background plasma density gradient on the wave propagation. At $t\Omega_{ce} = 100$, the waves look very similar in Figures 7a–7c; in all the cases the waves form near the magnetic equator with wave vector approximately parallel to **B** (wavefronts normal to **B**). At $t\Omega_{ce} = 200$, the wave vector remains approximately field aligned for $n_e \propto L^{-8}$ (Figure 7f), but the waves that have propagated away from the magnetic equator to $q \approx 0.3$ are more oblique for $n_e \propto L^{-4}$ (Figure 7e) and even more oblique for constant n_e (Figure 7d). At $t\Omega_{ce} = 300$, these differences are even clearer. Another difference is that the wave patches of the three simulations are located at different positions in the simulation domain. In Figures 7a, 7d, and 7g (constant n_e), the waves are located mainly in the region of larger r, and the wave vector is more oblique for large r than for smaller r. In Figures 7b, 7e, and 7h, the waves are less oblique and centered around $r = 1$. In Figures 7c, 7f, and 7i, waves occupy the whole simulation region, and the wave vectors are everywhere almost parallel to the background magnetic field.

In all three simulations, the plots of magnetic energy growth from the three cases are quite similar (not shown), and the waves saturate near $t\Omega_{ce} = 350$. For run 4, the maximum magnetic energy is about 1.87×10^{-4}; for run 5, it is 2.72×10^{-4}; and for run 6, it is 3.98×10^{-4} in normalized units. The initial growth of the waves is almost identical in each case. However, in run 4, the waves reach the boundary at $r = 1$ earlier than those in runs 5 and 6; these waves are then damped. In contrast, the waves in run 6 occupy the entire simulation domain, and less wave power gets damped at the boundaries.

To better understand these results, we performed similar simulations of whistler wave propagation in a cold plasma using the same hybrid code. The particle electron species are the same as in previous simulations except that the temperature of all particles is set to zero. We initialize these simulations with an initial

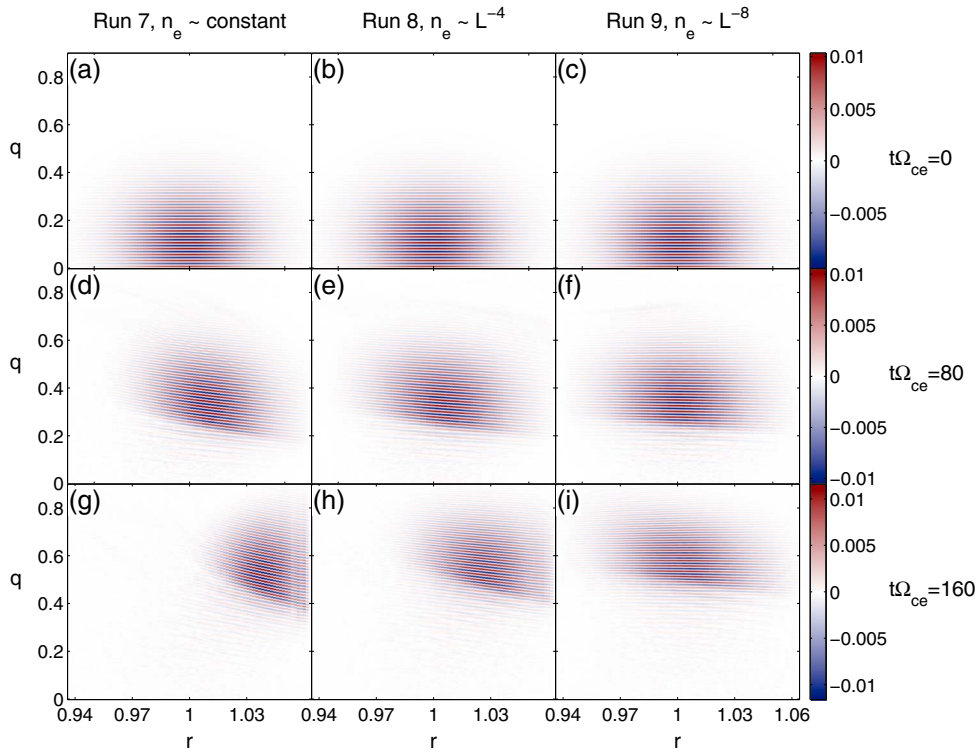

Figure 8. Like Figure 7, but for a cold plasma with an initial whistler wave perturbation.

whistler wave perturbation. Based on the fact that the waves in our hot plasma simulations have maximum instability in the parallel direction, the initial perturbations had **k** parallel to **B**. To do that, we needed to specify the wave frequency and amplitude. Based on the parameters simulated in previous sections, the wave frequency was chosen to be $\omega_0 = 0.4\Omega_{ce}$ and the amplitude was $0.01B_0$. We construct a parallel propagating plane wave with an envelope in q and r as described in Appendix A. Such initial perturbations form a traveling wave in the parallel direction with fixed frequency. We then let the wavefields and particle velocities evolve with time. This full wave approach gives us similar results to that of a ray tracing code.

Similar to the simulations with hot electrons, we performed three simulations with all cold plasma for the three different plasma density profiles. Figure 8 shows the results of these simulations. The plots are laid out in the same way as in Figure 7. Comparing Figure 8 with Figure 7, there are significant similarities in the wave propagation. The negative density gradient keeps the wave vector from turning outward. To understand the difference quantitatively, we then Fourier transformed the magnetic wavefield in **k** space. For $t\Omega_{ce} = 300$ (Figures 7g–7i), we obtained $\bar{k}_\perp$ and $\bar{k}_\parallel$ at which the wave power is maximum and calculated the angle between background magnetic field and wave vector θ_{kB}. For run 7, θ_{kB} is 20.1° in Figure 8d and 42.6° in Figure 8g; for run 8, θ_{kB} is 19.7° in Figure 8e and 24.1° in Figure 8h; finally for run 9, θ_{kB} is almost 0° at any time.

Note that the waveform in Figure 8 is a single smooth Gaussian traveling wave packet, while in Figure 7 there are many self-coherent wave packets. Coherence length of chorus waves is still a subject under investigation.

4. Discussion and Summary

We presented self-consistent simulations of whistler mode waves in 2-D Cartesian, 1-D dipole, and 2-D dipole coordinate systems. Our model used anisotropic electrons as particles to excite whistler waves, additional warm particles to provide inertia and a cold inertialess electron fluid. The ions are immobile. We derived a dispersion relation for this model and compared with WHAMP. We found that the error between our model and WHAMP for the parameters used in all of our simulations is around 17.5%. The frequency and

wave vector obtained from the simulation in 2-D Cartesian coordinates agree with predictions by WHAMP, and the comparison with a full dynamics model validates our model.

One-dimensional simulations in a dipole field were performed for both a full-scale system and a one-fourteenth scaled-down system. Both simulations show that the waves are generated near the magnetic equator and propagate to higher latitudes. The waves grow as they propagate. The waves are right-hand polarized near the generation region. In the scaled-down system, a rising tone is observed along the magnetic field line. The frequency sweep rate obtained from the simulation is $6.25 \times 10^{-3}\,\Omega_{ce}^2$, which agrees very well with the estimation of frequency sweep rate in equation (50) of *Omura et al.* [2008]. However, the frequency sweep rate is about 2 orders of magnitude greater than that observed. The huge difference can be explained by the large wave amplitude in our simulation. The frequency sweep rate is proportional to the wave energy saturation level. Due to limited computational resources, we used parameters for whistler waves that yield a much stronger instability than normally observed; thus, the wave amplitude is much greater, leading to a much greater frequency sweep rate. However, in the full-scale simulation, rising tones are not observed. *Katoh and Omura* [2013] investigated the effect of background magnetic field inhomogeneity on the generation process of chorus waves. With smaller inhomogeneity (background gradients), the threshold of wave amplitude for nonlinear growth is smaller. Thus, it should be easier to observe the rising tones with smaller inhomogeneity. However, *Katoh and Omura* [2013] reported that in the simulation with smallest inhomogeneity, the wave spectrum is broadband similar to that of hiss waves. These broadband waves consist of a group of waves with rising tones that emerge easily in the equatorial region. This may be an explanation for the character of the wave spectrum observed in our full-scale simulation. The inhomogeneity of run 2 is the same as that of the Earth's dipole field which is very small compared to that of most nonlinear simulations in the literature. Thus, in the scaled-down simulation, we observed chorus waves with discrete elements and rising tones, and the broadband whistler waves we observed in run 2 are possibly a group of chorus elements. In order to observe chorus waves in the full-scale simulation, we should probably use a smaller plasma beta that would lead to weaker whistler instability such that the discrete whistler elements would probably be more distinct.

To our knowledge, this is the first first-principle 2-D self-consistent simulation of whistler waves in a dipole field. First, we set the background plasma density to be constant along r so that the inhomogeneity is solely due to the dipole magnetic field (run 4). We found that the waves are generated with the wave vector parallel to the background magnetic field near the equatorial plane. The frequency range is within the predictions by WHAMP. As the waves propagate, the wave vector turns outward to greater L shell. The waves are more oblique at higher magnetic latitudes.

We then varied the total plasma density with respect to L to investigate the effect of a gradient in plasma density along L on chorus propagation. Two simulations were performed, run 5 with the total plasma density varying as L^{-4} and run 6 with density varying as L^{-8}. The waves are generated near the magnetic equator in the same fashion as run 4, and the wave power spectra look very similar. However, as the waves propagate to higher magnetic latitudes, the wave vector becomes less oblique when the density decreases with respect to r. In run 6, the wave vector remains roughly parallel along the center L shell. An even more dramatically decreased density than run 6 could lead to a wave vector turning inward toward the Earth.

To better understand the results from runs 4 to 6, we ran cold plasma simulations initialized with a whistler wave packet. The results from runs 7 to 9 are similar to those of runs 4 to 6, showing that the wave propagation can be explained based on cold plasma theory. Based on the calculation of θ_{kB} for runs 7–9, the maximum angle between the wave vector and background magnetic field is within 45°. Note, however, that runs 7–9 assume a single coherent whistler mode wave packet, while in runs 4–6 we observe several chorus patches with self-maintained coherence.

Features of Figures 7 and 8 agree with results from whistler ray tracing [*Inan and Bell*, 1977; *Chen et al.*, 2009, and private communication]. The wave vector **k** turns toward the direction of the density gradient, but away from the gradient of the magnetic field. The resulting turning of **k** is a balance between these two tendencies. With a constant plasma density, the wave vector will rotate toward greater L shell. As the density gradient increases (Figures 7b, 7e, and 7h; 7c, 7f, and 7i; 8b, 8e, and 8h; and 8c, 8f, and 8i), this rotation decreases and stops. Presumably the rotation would be inward for an even larger gradient.

Our model excludes $E_\parallel$. This is adequate for 1-D simulations for which the waves propagate parallel to the background magnetic field. However, $E_\parallel$ becomes more important for wave excitation in two dimensions. With our parameters, WHAMP predicts that the most unstable mode is in the parallel direction near the equatorial region, which is favorable for our model. But neglecting $E_\parallel$ has modified the whole unstable region in k space as can be seen from Figure 2 (there is a difference between the results from WHAMP and our model for oblique propagation.). In addition, neglecting $E_\parallel$ leads to the fact that there is no Landau damping in our system. Also, *Omura et al.* [2009] suggests that $E_\parallel$ might be essential for damping of whistler waves at $0.5\Omega_{ce}$. The effect of $E_\parallel$ is an important subject that will be addressed in future studies. While our model has this limitation, overall our simulations agree very well with observations and results of other models.

Appendix A: Initialization of a Traveling Whistler Wave Packet

Assuming that the perturbation has a plane waveform propagating in the q direction with a Gaussian envelope in both q and r directions, the real parts of the perturbed velocity of particles in the r and s directions at $t = 0$ are

$$\tilde{v}_{r,m} = \tilde{v}_0 \cos\phi_m e^{-\left(\frac{q_m-\tilde{q}_0}{\tilde{w}_q}\right)^2} e^{-\left(\frac{r_m-\tilde{r}_0}{\tilde{w}_r}\right)^2}, \tag{A1a}$$

$$\tilde{v}_{s,m} = -\tilde{v}_0 \sin\phi_m e^{-\left(\frac{q_m-\tilde{q}_0}{\tilde{w}_q}\right)^2} e^{-\left(\frac{r_m-\tilde{r}_0}{\tilde{w}_r}\right)^2}, \tag{A1b}$$

where m is the particle index, $\tilde{v}_{r,m}$ ($\tilde{v}_{s,m}$) is the velocity perturbation of particles in the r (s) direction, $\tilde{v}_0 = 0.01$ is the amplitude of the perturbation, q_m (r_m) is the position of the mth particle in the q (r) direction, $\tilde{q}_0$ ($\tilde{r}_0$) is the center of the Gaussian perturbation in the q (r) direction, $\tilde{w}_q$ ($\tilde{w}_r$) is the width of the Gaussian perturbation in the q (r) direction, and ϕ_m is the phase of the perturbation at the particle position, which depends on q_m. To get ϕ_m, we first calculate the wave phase at the grid points, ϕ_i, where i is the grid index in the q direction, and then interpolate the values on the grid to the particle position. At all r values, we use the phase for grid points calculated at the central field line ($r = \tilde{r}_0$) so that the initial waves are parallel propagating. We integrate ϕ_i from grid point i to grid point $i + 1$, based on the WKB approximation that the scale of spatial variation is greater than the wavelength so that the wave number can be considered constant between adjacent grid points, using these equations (in normalized units):

$$\phi_{i+1} = \phi_i + k_{\parallel,\mathrm{mid}} h_{1,\mathrm{mid}} \Delta q, \tag{A2}$$

where

$$k_{\parallel,\mathrm{mid}} = \sqrt{\frac{(1-\bar{n}_c)\omega_0}{B_{\mathrm{mid}}(1-\omega_0/B_{0,\mathrm{mid}})} + \frac{\bar{n}_c\omega_0}{B_{\mathrm{mid}}}}, \tag{A3a}$$

$$B_{\mathrm{mid}} = 0.5 * (B_{i,j_{\mathrm{mid}}} + B_{i+1,j_{\mathrm{mid}}}), \tag{A3b}$$

$$h_{1,\mathrm{mid}} = 0.5 * (h_{1,i,j_{\mathrm{mid}}} + h_{1,i+1,j_{\mathrm{mid}}}), \tag{A3c}$$

j_{mid} is the index of the center L shell and h_1 denotes the curvilinear scaling factor for q [*Hu and Denton*, 2009]. The quantity $k_{\parallel,\mathrm{mid}}$ is the local wave number at the particle position given the constant wave frequency based on (4). Based on (A1), the perturbation in the magnetic field on the grid is as follows:

$$\tilde{B}_{r,i,j} = k_{\parallel,i}(1 - B_{i,j_{\mathrm{mid}}}/\omega_0)\tilde{v}_0 \cos\phi_{i,j_{\mathrm{mid}}} e^{-\left(\frac{q_i-\tilde{q}_0}{\tilde{w}_q}\right)^2} e^{-\left(\frac{r_j-\tilde{r}_0}{\tilde{w}_r}\right)^2}, \tag{A4a}$$

$$\tilde{B}_{s,i,j} = k_{\parallel,i}(1 - B_{i,j_{\mathrm{mid}}}/\omega_0)\tilde{v}_0 \cos\phi_{i,j_{\mathrm{mid}}} e^{-\left(\frac{q_i-\tilde{q}_0}{\tilde{w}_q}\right)^2} e^{-\left(\frac{r_j-\tilde{r}_0}{\tilde{w}_r}\right)^2}. \tag{A4b}$$

Acknowledgments
Work at Dartmouth College was funded by NSF grant AGS-1155930 and NASA grants NNX13AD65G and NNX08AM58G. This work was also partially supported at Dartmouth by JHU/APL under NASAs prime contract NAS5-01072, under ECT (967399) subcontract from UNH and EFW (922613) subcontract from UMN. The work at Auburn University was supported by NSF grant 1303623 and NASA grant NNX13AD62G. Data to show the results of the hybrid simulations are accessible by contacting Shuo Wu. Data to show the results of the full particle simulations can be obtained by contacting Kaijun Liu. We thank Jay Johnson and Jacob Bortnik for useful conversations.

Michael Balikhin thanks the reviewers for their assistance in evaluating this paper.

References

Bortnik, J., R. M. Thorne, and N. P. Meredith (2008), The unexpected origin of plasmaspheric hiss from discrete chorus emissions, *Nature*, *452*(7183), 62–66, doi:10.1038/nature06741.

Burtis, W. J., and R. A. Helliwell (1976), Magnetospheric chorus: Occurrence patterns and normalized frequency, *Planet. Space Sci.*, *24*, 1007–1024, doi:10.1016/0032-0633(76)90119-7.

Cattell, C., et al. (2008), Discovery of very large amplitude whistler-mode waves in Earth's radiation belts, *Geophys. Res. Lett.*, *35*, L01105, doi:10.1029/2007GL032009.

Chen, L., J. Bortnik, R. M. Thorne, R. B. Horne, and V. K. Jordanova (2009), Three-dimensional ray tracing of VLF waves in a magnetospheric environment containing a plasmaspheric plume, *Geophys. Res. Lett.*, *36*, L22101, doi:10.1029/2009GL040451.

Cully, C. M., J. W. Bonnell, and R. E. Ergun (2008), THEMIS observations of long-lived regions of large-amplitude whistler waves in the inner magnetosphere, *Geophys. Res. Lett.*, *35*, L17S16, doi:10.1029/2008GL033643.

Cully, C. M., V. Angelopoulos, U. Auster, J. Bonnell, and O. Le Contel (2011), Observational evidence of the generation mechanism for rising-tone chorus, *Geophys. Res. Lett.*, *38*, L01106, doi:10.1029/2010GL045793.

Denton, R. E., and Y. Hu (2009), Symmetry boundary conditions, *J. Comput. Phys.*, *228*(13), 4823–4835, doi:10.1016/j.jcp.2009.03.033.

Draganov, A. B., U. S. Inan, V. S. Sonwalkar, and T. F. Bell (1992), Magnetospherically reflected whistlers as a source of plasmaspheric hiss, *Geophys. Res. Lett.*, *19*(3), 233–236.

Gendrin, R. (1961), Le guidage des whistlers par le champ magnetique, *Planet. Space Sci.*, *5*, 274–282.

Helliwell, R. A. (1965), *Whistlers and Related Ionospheric Phenomenon*, Stanford Univ. Press, Stanford, Calif.

Helliwell, R. A. (1967), A theory of discrete VLF emissions from magnetosphere, *J. Geophys. Res.*, *72*(19), 4773–4790.

Hikishima, M., S. Yagitani, Y. Omura, and I. Nagano (2009), Full particle simulation of whistler-mode rising chorus emissions in the magnetosphere, *J. Geophys. Res.*, *114*, A01203, doi:10.1029/2008JA013625.

Hu, Y., and R. E. Denton (2009), Two-dimensional hybrid code simulation of electromagnetic ion cyclotron waves in a dipole magnetic field, *J. Geophys. Res.*, *114*, A12217, doi:10.1029/2009JA014570.

Hu, Y., R. E. Denton, and J. R. Johnson (2010), Two-dimensional hybrid code simulation of electromagnetic ion cyclotron waves of multi-ion plasmas in a dipole magnetic field, *J. Geophys. Res.*, *115*, A09218, doi:10.1029/2009JA015158.

Inan, U. S., and T. F. Bell (1977), The plasmapause as a VLF wave guide, *J. Geophys. Res.*, *82*(19), 2819–2827.

Katoh, Y., and Y. Omura (2007), Computer simulation of chorus wave generation in the Earth's inner magnetosphere, *Geophys. Res. Lett.*, *34*, L03102, doi:10.1029/2006GL028594.

Katoh, Y., and Y. Omura (2013), Effect of the background magnetic field inhomogeneity on generation processes of whistler-mode chorus and broadband hiss-like emissions, *J. Geophys. Res. Space Physics*, *118*, 4189–4198, doi:10.1002/jgra.50395.

Katoh, Y. (2014), A simulation study of the propagation of whistler-mode chorus in the Earth's inner magnetosphere, *Earth Planets Space*, *66*, 6, doi:10.1186/1880-5981-66-6.

Kennel, C. F., and H. E. Petschek (1966), Limit on stably trapped particle fluxes, *J. Geophys. Res.*, *71*(1), 1–28.

Lee, W. W., and H. Okuda (1978), A simulation model for studying low-frequency microinstabilities, *J. Comput. Phys.*, *26*, 139–152.

Li, W., J. Bortnik, R. M. Thorne, and V. Angelopoulos (2011a), Global distribution of wave amplitudes and wave normal angles of chorus waves using THEMIS wave observations, *J. Geophys. Res.*, *116*, A12205, doi:10.1029/2011JA017035.

Li, W., R. M. Thorne, J. Bortnik, Y. Y. Shprits, Y. Nishimura, V. Angelopoulos, C. Chaston, O. Le Contel, and J. W. Bonnell (2011b), Typical properties of rising and falling tone chorus waves, *Geophys. Res. Lett.*, *38*, L14103, doi:10.1029/2011GL047925.

Liu, K., S. P. Gary, and D. Winske (2011a), Excitation of magnetosonic waves in the terrestrial magnetosphere: Particle-in-cell simulations, *J. Geophys. Res.*, *116*, A07212, doi:10.1029/2010JA016372.

Liu, K., S. P. Gary, and D. Winske (2011b), Excitation of banded whistler waves in the magnetosphere, *Geophys. Res. Lett.*, *38*, L14108, doi:10.1029/2011GL048375.

Naitou, H., S. Tokuda, and T. Kamimura (1979), On boundary conditions for a simulation plasma in a magnetic field, *J. Comput. Phys.*, *33*, 86–101.

Nishimura, Y., et al. (2010), Identifying the driver of pulsating aurora, *Science*, *330*(6000), 81–84, doi:10.1126/science.1193186.

Nunn, D. (1974), A self-consistent theory of triggered VLF emissions, *Planet. Space Sci.*, *22*, 349–378.

Nunn, D., and Y. Omura (2012), A computational and theoretical analysis of falling frequency VLF emissions, *J. Geophys. Res.*, *117*, A08228, doi:10.1029/2012JA017557.

Omura, Y., Y. Katoh, and D. Summers (2008), Theory and simulation of the generation of whistler-mode chorus, *J. Geophys. Res.*, *113*, A04223, doi:10.1029/2007JA012622.

Omura, Y., M. Hikishima, Y. Katoh, D. Summers, and S. Yagitani (2009), Nonlinear mechanisms of lower-band and upper-band VLF chorus emissions in the magnetosphere, *J. Geophys. Res.*, *114*, A07217, doi:10.1029/2009JA014206.

Ronnmark, K. (1983), Computation of the dielectric tensor of a Maxwellian plasma, *Plasma Phys. Controlled Fusion*, *25*(6), 699–701.

Santolík, O., D. A. Gurnett, J. S. Pickett, J. Chum, and N. Cornileau-Wehrlin (2009), Oblique propagation of whistler mode waves in the chorus source region, *J. Geophys. Res.*, *114*, A00F03, doi:10.1029/2009JA014586.

Santolík, O., C. A. Kletzing, W. S. Kurth, G. B. Hospodarsky, and S. R. Bounds (2014), Fine structure of large-amplitude chorus wave packets, *Geophys. Res. Lett.*, *41*, 293–299, doi:10.1002/2013GL058889.

Summers, D., B. Ni, N. P. Meredith, R. B. Horne, R. M. Thorne, M. B. Moldwin, and R. R. Anderson (2008), Electron scattering by whistler mode ELF hiss in plasmaspheric plumes, *J. Geophys. Res.*, *113*, A04219, doi:10.1029/2007JA012678.

Tao, X. (2014), A numerical study of chorus generation and the related variation of wave intensity using the DAWN code, *J. Geophys. Res. Space Physics*, *119*, 3362–3372, doi:10.1002/2014JA019820.

Tao, X., Q. Lu, S. Wang, and L. Dai (2014), Effects of magnetic field configuration on the day night asymmetry of chorus occurrence rate: A numerical study, *Geophys. Res. Lett.*, *41*, 6577–6582, doi:10.1002/2014GL061493.

Thorne, R. M. (2010), Radiation belt dynamics: The importance of wave-particle interactions, *Geophys. Res. Lett.*, *37*, L22107, doi:10.1029/2010GL044990.

Thorne, R. M., B. Ni, X. Tao, R. B. Horne, and N. P. Meredith (2010), Scattering by chorus waves as the dominant cause of diffuse auroral precipitation, *Nature*, *467*(7318), 943–946, doi:10.1038/nature09467.

Thorne, R. M., et al. (2013), Rapid local acceleration of relativistic radiation-belt electrons by magnetospheric chorus, *Nature*, *504*, 411–414, doi:10.1038/nature12889.

Trakhtengerts, V. Y. (1995), Magnetosphere cyclotron maser: Backward wave oscillator generation regime, *J. Geophys. Res.*, *100*(A9), 17,205–17,210.

Trakhtengerts, V. Y., A. G. Demekhov, E. E. Titova, B. V. Kozelov, O. Santolik, E. Macusova, D. Gurnett, J. S. Pickett, M. J. Rycroft, and D. Nunn (2007), Formation of VLF chorus frequency spectrum: Cluster data and comparison with the backward wave oscillator model, *Geophys. Res. Lett.*, *34*, L02104, doi:10.1029/2006GL027953.

Tsurutani, B. T., and E. J. Smith (1974), Postmidnight chorus: A substorm phenomenon, *J. Geophys. Res.*, *79*(1), 118–127, doi:10.1029/JA079i001p00118.

Watt, C. E. J., A. W. Degeling, R. Rankin, K. R. Murphy, I. J. Rae, and H. J. Singer (2011), Ultralow-frequency modulation of whistler-mode wave growth, *J. Geophys. Res.*, *116*, A10209, doi:10.1029/2011JA016730.

Wilson, L. B., III, C. A. Cattell, P. J. Kellogg, J. R. Wygant, K. Goetz, A. Breneman, and K. Kersten (2011), The properties of large amplitude whistler mode waves in the magnetosphere: Propagation and relationship with geomagnetic activity, *Geophys. Res. Lett.*, *38*, L17107, doi:10.1029/2011GL048671.

Woodroffe, J. R., and A. V. Streltsov (2014), Hybrid simulation of whistler excitation by electron beams in two-dimensional non-periodic domains, *J. Comput. Phys.*, *276*, 468–478, doi:10.1016/j.jcp.2014.06.055.

Wu, S., R. E. Denton, and W. Li (2013), Effects of cold electron density on the whistler anisotropy instability, *J. Geophys. Res. Space Physics*, *118*, 765–773, doi:10.1029/2012JA018402.